AIAA 99-0721

Laser-Induced Fluorescence Thermometry of a Weakly Ionized Radio-Frequency Plasma

Wim Ruyten, Michael S. Smith, and Linwood L. Price
Sverdrup Technology, Inc., AEDC Group
Arnold Engineering Development Center
Arnold Air Force Base, Tennessee 37389-4300

37th AIAA Aerospace Sciences Meeting & Exhibit
January 11-14, 1999 / Reno, NV

REPORT DOCUMENTATION PAGE

Form Approved
OMB No. 0704-0188

1. AGENCY USE ONLY *(Leave blank)*	2. REPORT DATE	3. REPORT TYPE AND DATES COVERED
	Jan 11, 1999	Conference Paper, Period 01/01/98-12/31/98

4. TITLE AND SUBTITLE
AIAA Paper 99-0721:
Laser-Induced Fluorescence Thermometry of a Weakly Ionized Radio-Frequency Plasma

5. FUNDING NUMBERS
AEDC Job 3328

6. AUTHOR(S)
Wim Ruyten, Michael S. Smith, and Linwood L. Price

7. PERFORMING ORGANIZATION NAME(S) AND ADDRESS(ES)
Sverdrup Technology, Inc., AEDC Group
Arnold Engineering Development Center
Arnold AFB, TN 37389-4300

8. PERFORMING ORGANIZATION REPORT NUMBER
AIAA paper 99-0721

9. SPONSORING/MONITORING AGENCY NAME(S) AND ADDRESS(ES)
Arnold AFB

10. SPONSORING/MONITORING AGENCY REPORT NUMBER
none

11. SUPPLEMENTARY NOTES
Paper was presented at 37th AIAA Aerospace Sciences Meeting & Exhibit, January 11-14, 1999, Reno, Nevada

12a. DISTRIBUTION AVAILABILITY STATEMENT
Unclassified

12b. DISTRIBUTION CODE

13. ABSTRACT *(Maximum 200 words)*

Results are reported of two-line laser-induced fluorescence thermometry measurements in a weakly ionized, radio-frequency plasma. The work was performed in support of hypervelocity studies in the AEDC S1 Impact Range. Rotational temperatures of nitric oxide were determined to be in the range 1000-2000 K, based on excitation of two lines in the NO A-X (0,0) band. A data analysis procedure is described for separating the weak, laser-induced fluorescence signals from natural emission from the plasma. By comparing temperatures from a strong and a weak beam, it is demonstrated that optical saturation is avoided. A strong correlation is found between the PLIF-derived NO temperatures and the intensity of natural emission from the plasma. This correlation is used to estimate the temperature distribution in the plasma outside the region that was accessible to interrogation by the laser sheets.

14. SUBJECT TERMS
Laser-induced fluorescence; LIF; thermometry; radio-frequency plasma; hypervelocity research; hypersonic flow; drag reduction

15. NUMBER OF PAGES
10

16. PRICE CODE

17. SECURITY CLASSIFICATION OF REPORT	18. SECURITY CLASSIFICATION OF THIS PAGE	19. SECURITY CLASSIFICATION OF ABSTRACT	20. LIMITATION OF ABSTRACT
Unclassified	Unclassified	Unclassified	Non

LASER-INDUCED FLUORESCENCE THERMOMETRY OF A WEAKLY IONIZED RADIO-FREQUENCY PLASMA*

Wim Ruyten,† Michael S. Smith,† and Linwood L. Price‡
Sverdrup Technology, Inc./AEDC Group
Arnold AFB, TN 37389-4300

ABSTRACT

Results are reported of two-line laser-induced fluorescence thermometry measurements in a weakly ionized, radio-frequency plasma. The work was performed in support of hypervelocity studies in the AEDC S1 Impact Range. Rotational temperatures of nitric oxide were determined to be in the range 1000-2000 K, based on excitation of two lines in the NO A-X (0,0) band. A data analysis procedure is described for separating the weak, laser-induced fluorescence signals from natural emission from the plasma. By comparing temperatures from a strong and a weak beam, it is demonstrated that optical saturation is avoided. A strong correlation is found between the PLIF-derived NO temperatures and the intensity of natural emission from the plasma. This correlation is used to estimate the temperature distribution in the plasma outside the region that was accessible to interrogation by the laser sheets.

1.0 INTRODUCTION

One of the methods that has been under investigation for the reduction of drag on hypersonic aircraft is the use of a plasma generator to ionize the airflow around the aircraft. Evidence for such a reduction in drag has been inferred by Russian researchers from experiments in which the shock-standoff distance for a spherical projectile fired through a weakly ionized plasma was several times the estimated thermal value.[1,2] These results are not well understood. In particular, it is not clear what the relative contributions are of thermal heating on the one hand, and ionization on the other. A series of experiments was undertaken at the Arnold Engineering Development Center to gain further insight into the pertinent mechanisms of such plasma phenomena.

The experiments were performed in AEDC's S1 Hypervelocity Impact Range. A radio-frequency generator was used to create weakly ionized plasma in about 15-40 torr of air. Spherical projectiles with diameters of 9.5 and 19.1 mm were fired through the plasma, and a number of diagnostic instruments were used to investigate the resulting interactions. A comprehensive description of these experiments and their results may be found in another paper, also presented at this conference,[3] and elsewhere.[4,5] The purpose of the present paper is to describe, in detail, the results of planar laser-induced fluorescence (PLIF) experiments in the plasma region. These experiments were performed to determine the rotational temperature of nitric oxide in the plasma, based on the principle of two-line fluorescence thermometry. The results are compared with temperature measurements obtained by the use of thermocouples and by emission spectroscopy of N_2^+.

2.0 EXPERIMENTAL SETUP

The design of the experiment was motivated by the need to fire a projectile through the plasma region. For this reason, the electrode assembly inside of which the plasma was generated was mounted in a vacuum tank at the end of the S1 Hypervelocity Impact Range launcher. Figure 1 gives an overall view of the setup. Figure 2 shows a detailed schematic of the plasma region. The experiments

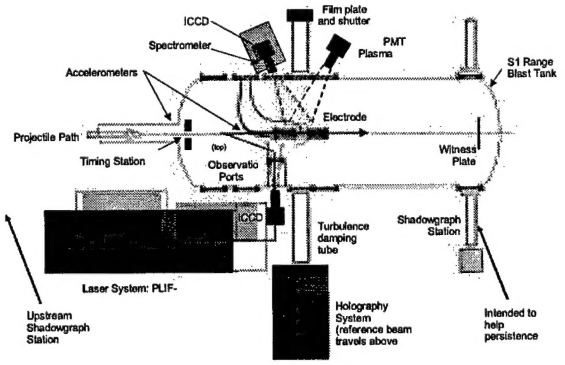

Fig. 1. Experimental setup.

---

* *The research reported herein was performed by the Arnold Engineering Development Center (AEDC), Air Force Materiel Command. Work and analysis for this research were performed by personnel of Sverdrup Technology, Inc., AEDC Group, technical services contractor for AEDC. Further reproduction is authorized to satisfy needs of the U. S. Government.*

† Senior Engineer, Member AIAA

‡ Senior Engineer

Approved for public release; distribution unlimited.

reported here were performed without a projectile launch. Instead, two overlapping laser sheets were directed along the length of the plasma, to allow the temperature distribution along the nominal projectile path to be mapped out by two-line fluorescence thermometry. A comb was placed in the laser sheets to break the sheets up into parallel bright and dark regions, for the purpose of separating laser-induced fluorescence emission from background emission from the plasma.

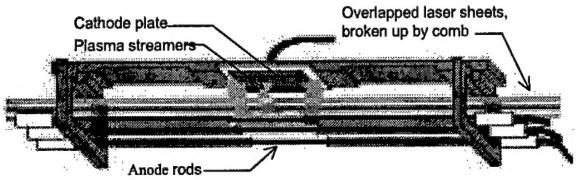

Fig. 2. Schematic of the electrode assembly.

Both excitation sources were Nd:YAG-pumped dye-laser systems. A frequency-doubled Spectra Physics® laser was used to pump a Rhodamine 590/610-based tunable dye laser, the output of which was frequency doubled and then mixed with the Nd:YAG fundamental to produce output at 225.716 nm. A frequency-tripled Continuum® Nd:YAG laser was used to pump a Coumarin-450 based tunable dye laser. Output from it was frequency doubled using a BBO crystal, yielding the required output at the second excitation wavelength, at 225.134 nm. The choice of excitation wavelengths is discussed in Section 3.0, as are further details of the PLIF system.

Two intensified, charge-coupled device cameras were used to image the resulting fluorescence at a resolution of 578 × 384 pixels each. Schott UG-5 filter glass was used to block scattered laser light and room light. The target species was nitric oxide, formed naturally in the plasma. Measurements were made during individual runs of the plasma generator. The device was limited to a duty cycle of 30 sec on and at least 300 sec off to prevent overheating of the generator electrodes. Even so, the appearance of the plasma was typically nonuniform and varied over the course of a run. Figure 3 shows a representative snapshot image, taken with one of the PLIF cameras, but without the laser sheets present. Three streamers are discernible as bright columns in the image: Two at the ends of the upper electrode and one to the left of the image center. The number of streamers was dependent on operating conditions.

In the experiments reported here, the plasma was generated in 30 torr of air by a modified induction heater power supply, rated at 5 kW, with a cycle frequency of 369 kHz. The upper electrode consisted of a 150-mm-long copper plate, which was biased negative relative to the lower electrode rods.

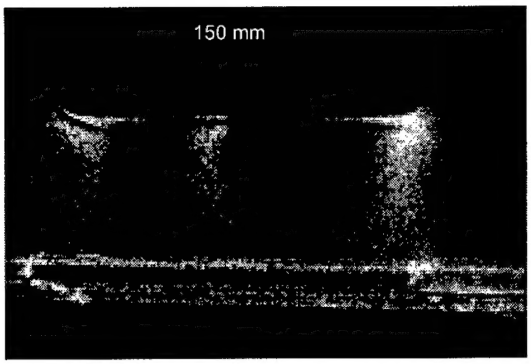

Fig. 3. Snapshot view of plasma.

3.0 LIF MEASUREMENTS

The principle of temperature measurement by two-line laser-induced fluorescence (LIF) is well known.[6-9] Let S_1 and S_2 be the LIF signals associated with excitation of the target species (in this case NO) by the two laser lines. Furthermore, let E_1 and E_2 be the pulse energies of the two lasers measured at the excitation volume. Then the ratio of the two LIF signals is given by

$$\frac{S_2}{S_1} = C_{21}\frac{E_2}{E_1}\frac{B_2}{B_1}\frac{2J_2''+1}{2J_1''+1}\exp\left(-\frac{\Delta\varepsilon_{21}}{kT}\right), \qquad (1)$$

where B_2 and B_1 are the Einstein coefficients for stimulated emission for the two lines, J_2'' and J_1'' are the rotational quantum numbers of the ground states of the two lines, k is Boltzmann's constant, T is the rotational temperature of the target species, and $\Delta\varepsilon_{21}$ is the energy separation between the two ground states. The constant C_{21} is an apparatus constant which is given, essentially, by the ratios of the detection efficiencies of the cameras that are used to image the LIF emissions from the plasma. Strictly speaking, C_{21} also depends on the line shapes of the two lasers. This dependence is neglected because the line shapes of the two lasers are nearly identical: Both have a line shape that is approximately gaussian, with a full-width at half maximum of 1.0 cm^{-1}. Also implicit in Eq. (1) are the assumptions that the two lasers are each tuned to the center of an absorption line, that attenuation of the laser sheets by absorption is negligible, and that the power density in the laser sheets is small enough that no optical saturation takes place. This last requirement is considered in more detail below, both from a theoretical and an experimental standpoint.

The choice of the two excitation lines is determined by the requirements that both lines have good separation from neighboring excitation lines, that both give strong LIF signals, and that the ratio in Eq. (1) have good temperature sensitivity. The latter requirement is satisfied if the energy separation $\Delta\varepsilon_{21}$ is on the order of, or larger

than, the thermal energy kT. Anticipating plasma temperatures in the range 1000-1500 K, a line pair was chosen with $\Delta\varepsilon_{21}$ = 1550 K. The two lines are the $R_{11} + Q_{21}(13.5)$ line ("line 1") at 225.716 nm and the $P_{21} + Q_{11}(28.5)$ line ("line 2") at 225.134 nm. Both are in the NO A-X (0,0) band. For these two lines, Eq. (1) can be inverted to give the temperature in terms of the two LIF signals as

$$T = \frac{-1550K}{\ln\left[\frac{S_2}{S_1}\Big/\left(2.825\times C_{21}\frac{E_2}{E_1}\right)\right]}. \qquad (2)$$

Pulse durations for both lasers were about 10 nsec. Both cameras were operated with a 300-nsec gate. A delay of 700 nsec was used between the two pulses to avoid overlap of the emission signal from the first laser with the gate-open time of the second pulse.

To estimate the onset of optical saturation, the following expression was used for the LIF-signal S of a spectral line:

$$S \propto 1-\exp(-\Re), \qquad (3)$$

where

$$\Re = \left(\frac{E}{hc\nu}\right)\left(\frac{\sigma_0}{A}\right)\left(\frac{\Delta\nu}{\Delta\nu_L}\right). \qquad (4)$$

Here, E is the energy of the laser pulse measured at the location of the excitation volume, $hc\nu$ is the energy of a laser photon, σ_0 is the line-center absorption cross-section of the transition, A is the area of the laser sheet in the excitation volume, $\Delta\nu$ is the line width of the transition, and $\Delta\nu_L$ is the line width of the laser. For the present purpose, the onset of optical saturation is defined as the pulse energy at which the quantity 1-exp(-$\Re$) in Eq. (3) deviates from its linear approximation (i.e., $\Re$) by precisely 10 percent. This occurs for the value $\Re$ = 0.215. In turn, this leads to the following requirements for the laser pulse energies E at the centers of the excitation volumes:

$$\begin{cases} E[mJ] \le 0.009\times A[mm^2],\ 225.716\,nm, \\ E[mJ] \le 0.0066\times A[mm^2],\ 225.134\,nm. \end{cases} \qquad (5)$$

Net pulse energies in the excitation volume were 0.65 mJ for the 225.716 line and 0.56 mJ for the 225.314 line. These values were measured without the comb that was used to break the laser sheets into parallel bright and dark bands. For these energies, Eqs. (5) implies that the cross-sectional area of the laser sheets in the excitation volume should be on the order of 85 mm^2 or larger. The size chosen was 25 mm × 3 mm for both sheets. It is confirmed experimentally in Section 5 that saturation is not a problem at these conditions.

The ratio E_2/E_1 from Eq. (1) of the two pulse energies at the excitation volume was measured indirectly, by measuring the pulse energies P_1 and P_2 of split-off portions of the two beams at the start of the common transmission optics. For each measurement (that is, for each pair of laser pulses), the ratio P_2/P_1 was then converted to the desired ratio E_2/E_1 according to

$$\frac{E_2}{E_1} = \frac{P_2}{P_1}\times\left(\frac{E_{2,ref}/P_{2,ref}}{E_{1,ref}/P_{1,ref}}\right). \qquad (6)$$

The quantities with a subscript "ref" are those measured at an initial reference condition.

4.0 DATA ANALYSIS

Figure 4 shows a typical pair of PLIF images from the plasma region. The direction of the laser sheets is left to right in both images. One strong beam and one weak beam are visible. The difference in beam intensities was an unintended consequence of the nonuniform energy distributions in the laser sheets. In the top and bottom of each image in Fig. 4, the plasma electrodes are visible, with the cathode at the top. Clearly, natural emission from the plasma is significant, particularly in the regions of the streamers. As in Fig. 3, three streamers may be discerned: two at the boundaries of the plasma, and one to the left of the image center. The streamer structure changes with

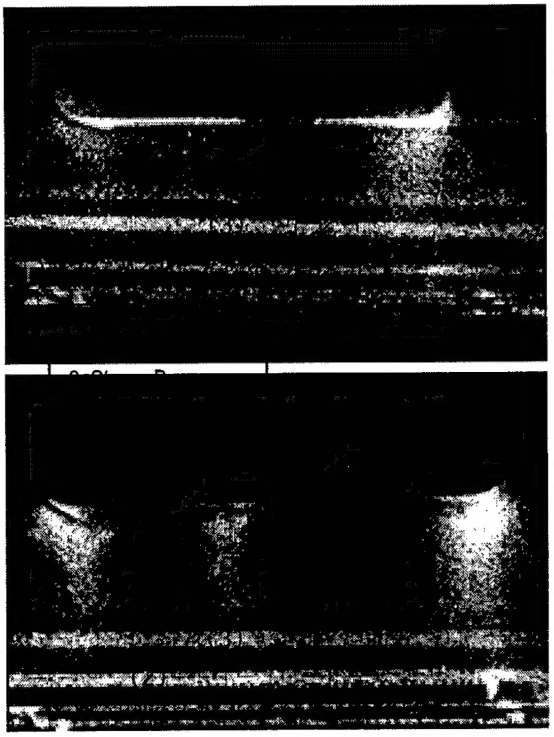

Fig. 4. Pair of PLIF images for Run 28.

time and from one set of images to the next. However, the structure is roughly constant over the 1-μsec period needed to acquire both images (700-nsec delay plus 300-nsec gate-open time).

The following procedure was followed for extracting net LIF signals from images such as those in Fig. 4. First, a geometric calibration was performed, by imaging a calibration target with both cameras. See Fig. 5, in which the bold lines form a square grid with linear cell dimensions of 25.4 mm. Next, the PLIF images were

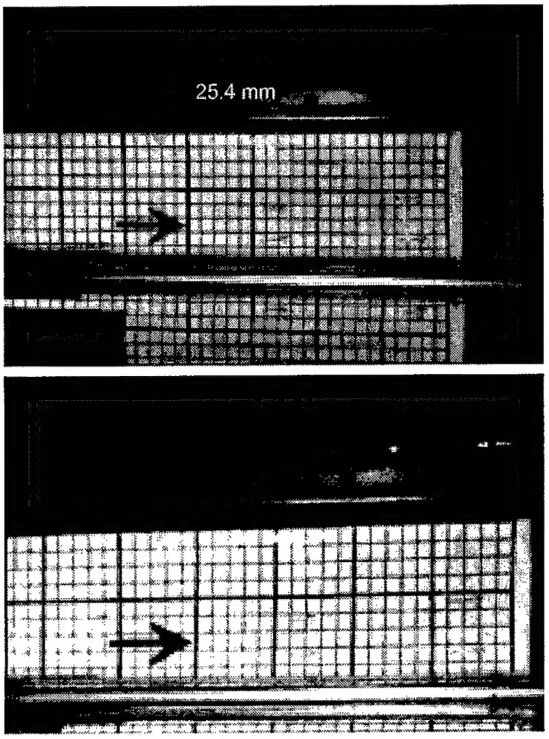

Fig. 5. Pair of geometric calibration images.

divided into 29 vertical bands each. This number was selected as a reasonable compromise between maintaining adequate spatial resolution along the direction of the laser sheets, while being able to average the weak LIF signals over a sufficiently wide region to ensure reasonable statistics. The boundaries of the bands were chosen such that a given band in the 225.716-nm image projects to the same width (6.0 mm) in the plasma as the corresponding band in the 225.134-nm image. Within each band, a single vertical profile was calculated, centered on the dark region between the strong and weak laser beams. A typical example is shown in Fig. 6. Each vertical profile was divided into bright and dark regions, referring to whether or not laser energy is present. Figure 6 indicates the locations of these boundaries. A quadratic curve (shown as a dashed line in Fig. 6) was fitted to the signals in the dark regions to obtain a baseline profile for natural emission from the plasma. The fitted baseline values were subtracted from the total signals to obtain net LIF emission profiles. From these, integrated LIF signal values were obtained, for the strong and weak beams separately, by summing the positive contributions in each region. The net integrated LIF signals are thus given by

$$S_{LIF} = \sum_{i \in bright} \max\left\{0, S_{i,total} - S_{i,fitted}\right\}. \quad (7)$$

Estimates of the standard deviations of these integrated LIF signal values were calculated according to

$$\Delta S_{LIF} = \sqrt{n_{bright}} \times \sigma_{dark}, \quad (8)$$

where n_{bright} is the number of points i, in either in the weak-beam or strong-beam regions, with a positive net signal value, and σ_{dark} is an estimate of the noise level of the net signal values in the dark regions, given by

$$\sigma_{dark} = \left\{ n_{dark}^{-1} \sum_{i \in dark} \left(S_{i,total} - S_{i,fitted}\right)^2 \right\}^{1/2}. \quad (9)$$

Here, n_{dark} is the number of points i on the net-signal profile that are located in a dark region. The assumption that is implicit in the estimation of the standard deviations ΔS_{LIF} from Eq.(8) is that the effective noise levels in the bright regions are the same as those in the dark regions. It is found below that they are actually somewhat higher.

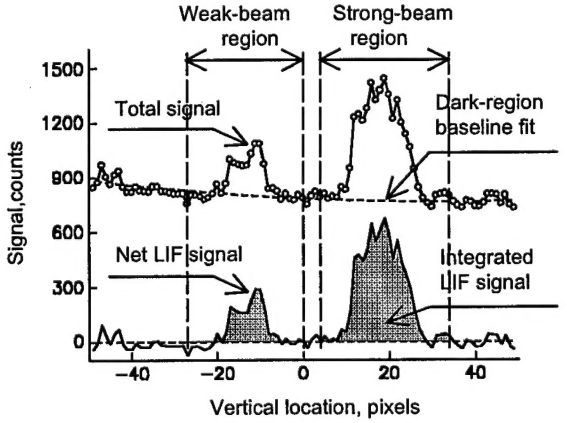

Fig. 6. Extraction of integrated LIF signals from vertical signal profiles.

Figure 7 shows overlays of all the vertical profiles that were extracted from the two images in Fig. 4. The fitted baselines have been subtracted. The data are plotted as a function of relative height in the plasma. The average value of the noise levels σ_{dark} from Eq. (9) for the 225.134-nm profiles is 35 counts, and 19 counts for the 225.716-nm profiles. Using Eq. (8), these values translate

to standard deviations for the LIF signals of about 190 counts for the integrated 225.314-nm LIF signals, and about 95 counts for the integrated 225.716-nm signals.

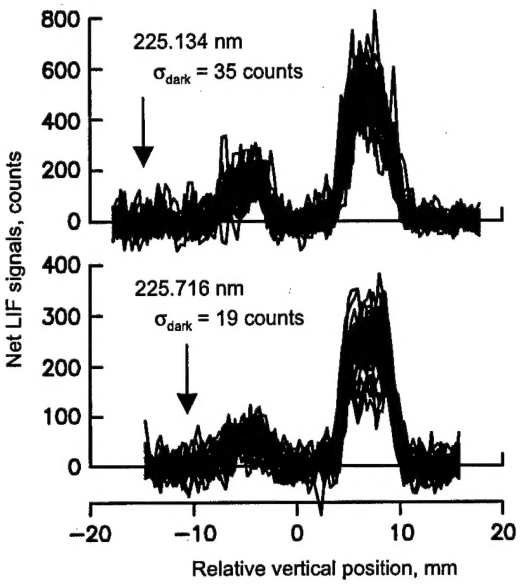

Fig. 7. Overlay of net LIF signal profiles for the images from Fig. 4.

Figure 8 shows axial profiles of the net, integrated LIF signals S_{LIF} from Eq. (7) for both the 225.134-nm and 225.716-nm images. For each wavelength, both a strong-beam and a weak-beam curve are shown. The estimated standard deviations are indicated. What remains to be done before these integrated LIF signals can be converted into temperature profiles is a calibration of the detection efficiency ratio C_{21} from Eq. (1). To accomplish this, two sets of images were taken in which, unlike in the actual PLIF measurements, gated both cameras on the same laser pulse. Subsequent extraction of the integrated PLIF signals was identical to that described above for the images shown in Fig. 4.

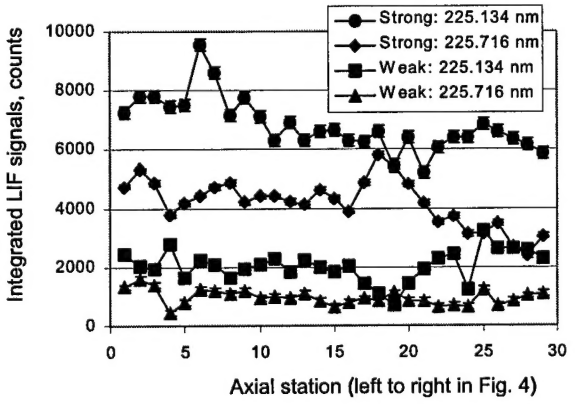

Fig. 8. Axial distribution of integrated LIF signals for the images from Fig. 4.

Figure 9 shows the results in the form of axial signal-ratio profiles. One set of curves was obtained with just the 225.716-nm laser beam entering the plasma region, the other with just the 225.134-nm beam. Both sets consist of a strong-beam ratio and a weak-beam ratio. As expected, the weak-beam ratios show a larger variance about an average value than do the strong-beam ratios. For both the strong and weak beams, the variances in signal ratios are larger, by factors of about 2-3, than the variances (shown as error bars in Fig. 9) calculated on the basis of the estimated standard deviations from Eqs. (8) and (9). This seems to indicate that the estimates of the standard deviations of the integrated signal values from Eq. (8) are low. Combining the data from Fig. 9, a single value, 1.93, was obtained for the detection efficiency ratio C_{21} from Eq. (1). The uncertainty in this value is estimated to be 0.05, or about 2.6 percent.

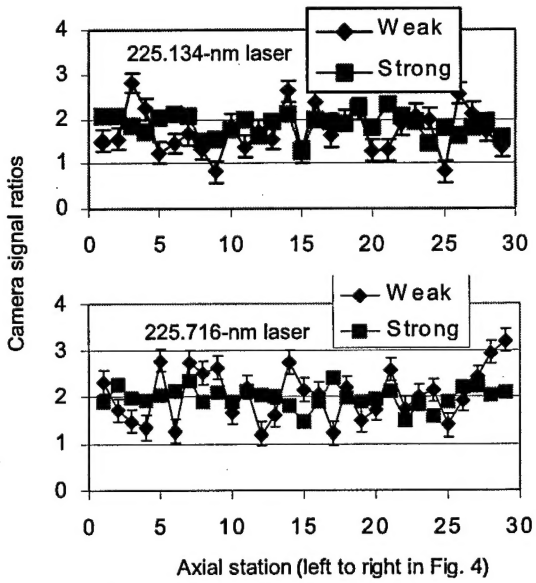

Fig. 9. LIF signal ratio calibration.

It is now possible to convert the integrated LIF signals S_{LIF} from Fig. 8 to axial temperature profiles with the help of Eqs. (2) and (6). Figure 10 shows the results, including error bars. For the strong beam in Fig. 4, one data point is plotted for each of the 29 axial locations that were selected. For the weak beam, only those data points are shown that have a calculated standard deviation of less than ±500 K. The limits of the error bars were calculated from the estimated standard deviations ΔS_{LIF} from Eq. (8) by replacing the signal ratios S_2/S_1 in Eq. (2) with the noise-corrupted ratios $(S_2+\Delta S_2)/(S_1-\Delta S_1)$ for the upper limits and $(S_2-\Delta S_2)/(S_1+\Delta S_1)$ for the lower limits. Ordinarily, this calculation would result in an

overestimate of the standard deviation of the ratios S_2/S_1 and, hence, of the deduced temperatures. In this case, the calculation is justified on the basis that the estimated standard deviations ΔS_{LIF} from Eq. (8) were found to be low in the calculation of the detection efficiency ratio C_{21} in the preceding paragraph.

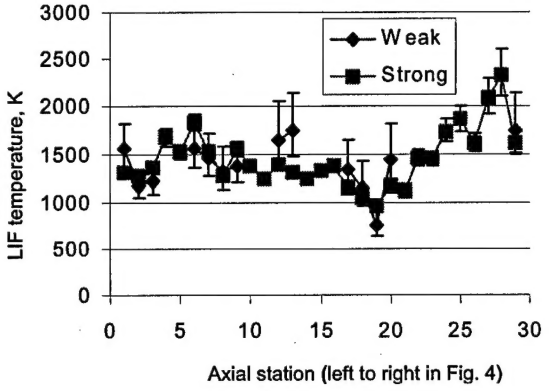

Fig. 10. Axial distribution of LIF-deduced temperatures in Fig. 4.

Finally, Fig. 11 shows axial profiles of the natural emission signals from the plasma. These values were obtained by evaluating the quadratic baseline fits (such as are shown in Fig. 6) at the center positions of the weak and strong laser beams. For each profile, a background value was subtracted, which was obtained from the low-signal region above the cathode plate (see Figs. 3 and 4). As will be seen in Section 5.0, the temperature profiles and the emission profiles are strongly correlated. Inspection of the emission distribution thus provides a qualitative temperature diagnostic.

5.0 DISCUSSION OF RESULTS

Summarized now are the results from a series of five plasma generator runs, Runs 27-31. For each of these, the location of the laser sheets and the comb are the same as in Fig. 4, which shows the results of the second of the five runs, Run 28.

Figure 12 shows the dual LIF-derived temperature profiles for the five runs. The weak-beam and strong-beam profiles are shown separately. For the weak beam, only data points with a calculated standard deviation of less than ±500 K are shown. Also shown for each run is the background–corrected profile of the natural plasma

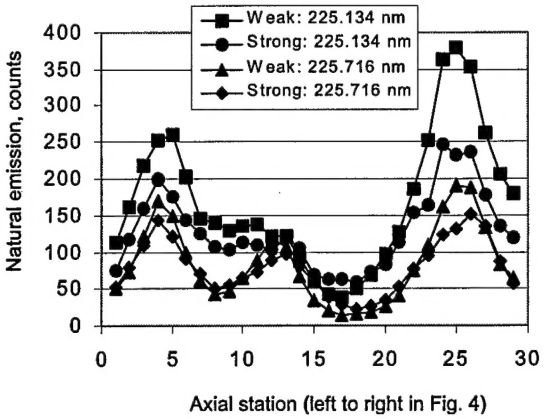

Fig. 11. Distribution of natural emission at the laser beam positions in Fig. 4.

emission, calculated at the center of the strong beam. The emission profiles are averages of the 225.134-nm and 225.716-nm images. Thus, temporal variations in plasma structure are averaged out in a manner that is similar to that which occurs when calculating the LIF-based temperature distributions from images which are separated in time by several hundred nanoseconds.

The first observation about the results in Fig. 12 is that the weak-beam temperatures are consistent with the strong-beam values within the calculated uncertainties. To be precise, for the 80 points in Fig. 12 for which both weak-beam and strong-beam temperatures are available, the weak-beam temperatures are higher than the strong-beam values by only 21 K on average. In fact, they should be somewhat higher, given the positive correlation between plasma emission and temperature that is found below. The consistency between the weak-beam and strong-beam temperatures confirms that optical saturation, with its accompanying nonlinearities, is not a problem, in agreement with the calculations in Section 3.0.

Second, the results in Fig. 12 show that there is a distinct correlation between the shapes of the temperature profiles and the shapes of the corresponding emission profiles. In particular, regions of elevated temperature coincide consistently with the streamer regions in the plasma, which are marked by elevated emission levels. Figure 13 quantifies this correlation by plotting the relative variations in temperature against the relative variations in emission intensity. Data from the five runs are combined into a single plot. For each run, the percent

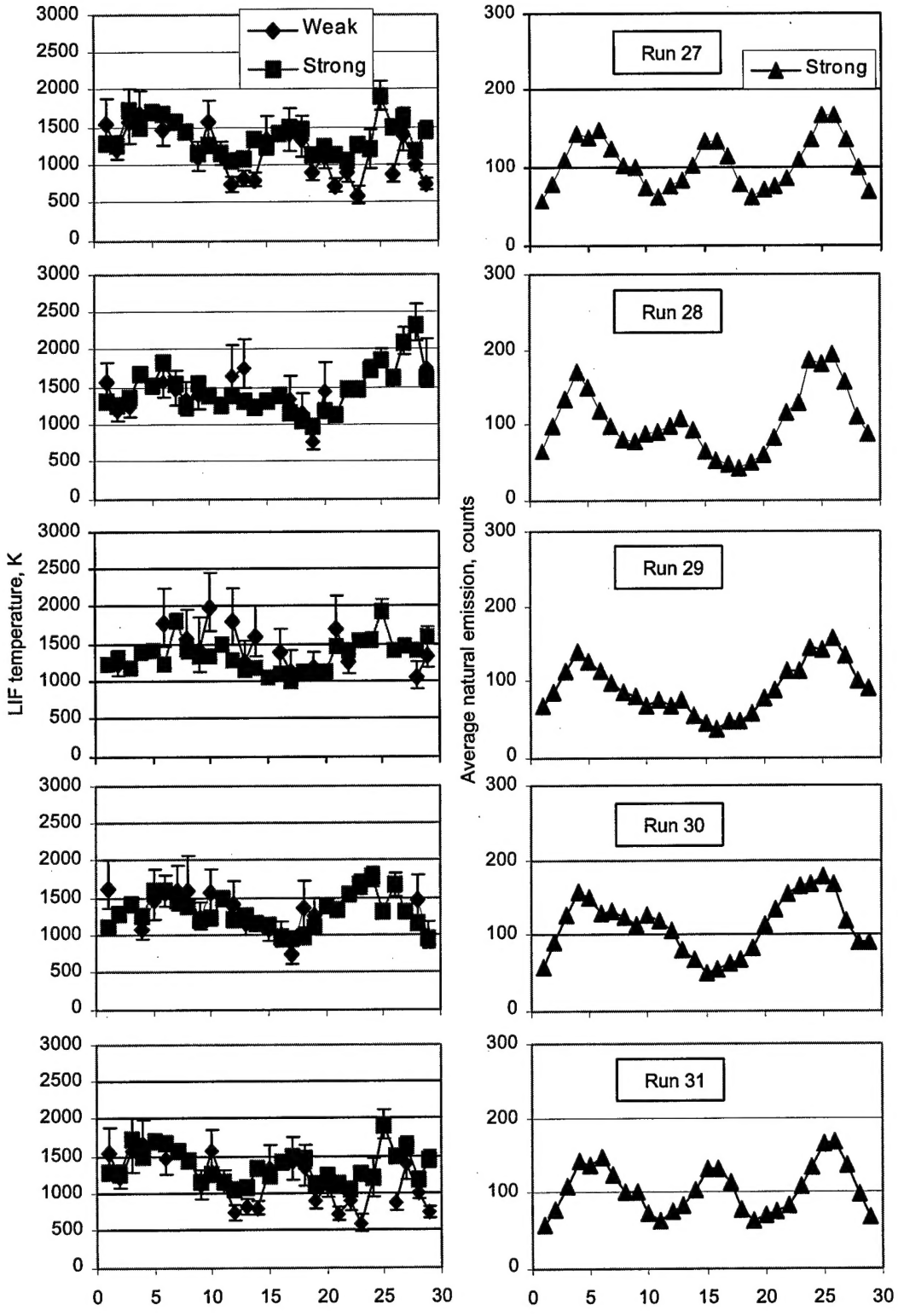

Fig. 12. Distributions of temperature and average natural emission for five runs.

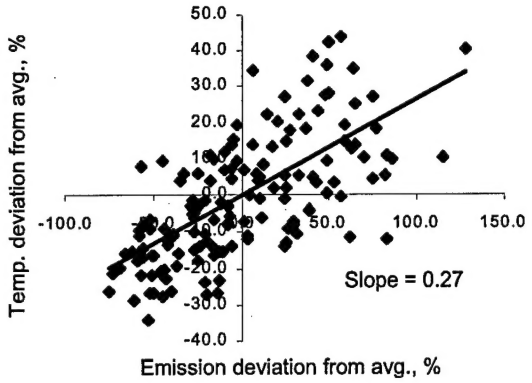

Fig. 13. Correlation between intensity variation and emission variation along strong beams.

deviations in temperature and emission are calculated relative to the average values per run. Despite the scatter of the data, a positive correlation between the two quantities is evident. A linear curve fit to the data in Fig. 13 gives a slope of 0.27 for this correlation. This implies that the temperature varies as the background-corrected emission intensity raised to the power 0.27. With this information, it is possible to estimate the temperature distribution in the whole plasma region from the emission distribution according to

$$T_{emis} = \overline{T}_{LIF} \times \left(E_{emis} / \overline{E}_{LIF} \right)^{0.27}, \qquad (10)$$

where E_{emis} is the emission intensity at an arbitrary point in the plasma, E_{LIF} is the average emission along the length of the laser sheets, and T_{LIF} is the average temperature along the length of the laser sheets. For the five runs from Fig. 12, this last value is 1368 K, with a one-sigma spread of 257 K (see Fig. 14).

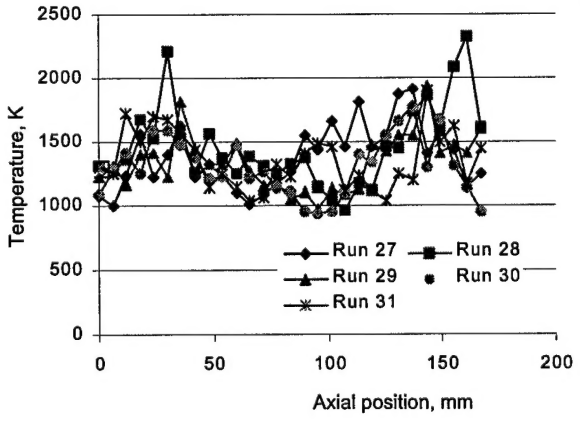

Fig. 14. Overlay of the strong-beam axial temperature profiles from Fig. 12.

Using Eq. (10), a series of vertical temperature profiles was calculated for the snapshot image from Fig. 3. First, the 225.134-nm image was remapped to overlay the 225.716-nm image. The two images were averaged and the average emission intensity, E_{emis} from Eq. (10), was calculated at the position of the strong laser beam in Fig. 4. Temperatures elsewhere in the plasma were then calculated using Eq. (10), with T_{LIF} = 1368 K. Results from this calculation are shown in Fig. 15. The range of temperatures is 630 to 2100 K, which is roughly the range of the data in Fig. 13 from which the correlation in Eq. (10) is derived. Of course, the temperatures in Fig. 15 are tentative, given the scatter in the data in Fig. 13. In addition, the emission from the plasma is a three-dimensional effect, whereas the LIF temperature values are essentially for a two-dimensional slice through the plasma.

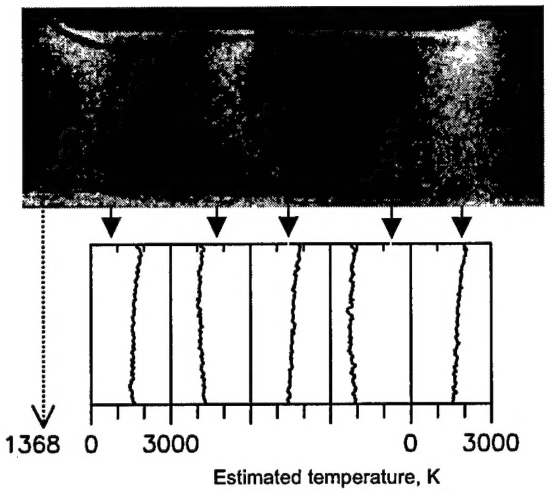

Fig. 15. Emission-based estimates of vertical temperature profiles in plasma.

6.0 CONCLUSIONS

Rotational temperatures of nitric oxide in a weakly ionized radio-frequency plasma were determined to be in the range 1000-2000 K by two-line laser-induced fluorescence thermometry. A positive correlation was observed between natural emission from the plasma and temperatures along the path of a 6-mm-high laser sheet. Based on this correlation, temperatures in other regions in the plasma were estimated to be in the range 630-2100 K, with the highest temperatures near the cathode. Consistent results for the LIF-derived temperatures were obtained for weak-beam and strong-beam excitation. This indicates that the power densities of the excitation light are small enough that optical saturation is avoided. The LIF-derived temperatures compare reasonably well with those derived by the use of thermocouples (1150 K) and by

emission spectroscopy of N_2^+ (700 K).[3] All three temperatures are too low to account for the observed shock-standoff distances in the experiments in which spherical projectiles were fired through the plasma.[3] This result appears to confirm the conclusions reached by Russian researchers,[1,2] namely that an as-yet not-understood plasma phenomenon is responsible for the apparent reduction in drag on projectiles fired through a plasma.

The combination of LIF-temperature measurements and the extrapolation of the LIF-based results to the entire region in the plasma offer the opportunity to provide realistic inputs for three-dimensional computational fluid dynamic calculations of the shock formation around a spherical projectile. Initial calculations of this sort indicate that the existence of vertical temperature gradients in the plasma may have a significant effect on the resulting shock shapes, and hence on the attribution of observed shock stand-off distances to either thermal or plasma effects.

ACKNOWLEDGMENTS

Many individuals have contributed to this effort. In particular, we thank Mike Forsythe, Joel Mansfield, Les Crosswy, and Peter Sherrouse for technical assistance, and Heard Lowry, Jim Drakes, and Wheeler McGregor for advice and assistance with analysis.

REFERENCES

1. Mishin, G. I., Serov, Yu. L., and Yavor, I. P., "Flow Around a Sphere Moving Supersonically in a Gas Discharge Plasma," Pis'ma Zh. Tekh. Fiz. (Soviet Technical Physics Letters), Vol. 17, June 12, 1991, pp. 65-72.
2. Bedin, A. P. and Mishin, G. I., "Ballistic studies of the Aerodynamic Drag on a Sphere in Ionized Air," Pis'ma Zh. Tekh. Fiz., Vol. 21, 1995, pp. 14-19.
3. Lowry, H., Stepanek, C., Crosswy, L., Sherrouse, P., Smith, M., Price, L., Ruyten, W., and Felderman, J., "Shock Structure of a Spherical Projectile in Weakly Ionized Air," AIAA Paper 99-0060, Reno, NV, January 1999.
4. Lowry, H., Blanks, J., Stepanek, C., Smith, M., Crosswy, L., Sherrouse, P., Felderman, J., and Wood, B., "Characterization of the Shock Structure of a Spherical Projectile in Weakly Ionized Air Through Ballistic Test Techniques," presented at the Second Weakly Ionized Gas Workshop, Norfolk, VA, April 24-25, 1998.
5. Blanks, James R. and Lowry, Heard S., "Supersonic Projectile Tests in a Weak Plasma," AEDC-TR-98-1, September 1998.
6. McMillin, B. K., Palmer, L. P., and Hanson, R. K., "Temporally Resolved, Two-Line Fluorescence Imaging of NO Temperature in a Transverse Jet in a Supersonic Cross Flow," *Appl. Opt.*, Vol. 32, 1993, pp. 7532-7545.
7. Lee, M. P., McMillin, B. K., and Hanson, R. K., "Temperature measurements in gases by use of planar laser-induced fluorescence imaging of NO," *Appl. Opt.*, Vol. 32, 1993, pp. 5379-5396.
8. Smith, M. S., Price, L. L., and Williams, W. D., "Laser-Induced Fluorescence Diagnostics Using a Two-Line Excitation Method," *AIAA Journal*, Vol. 31, 1993, pp. 478-482.
9. Ruyten, W. M., Smith, M. S., Price, L. L., and Williams, W. D., "Three-Line Fluorescence Thermometry of Optically Thick Shock-Tunnel Flow," *Appl. Opt.*, Vol. 37, 1998, pp. 2334-2339.